



Cite this: *J. Mater. Chem. C*, 2022, 10, 15386

## Two-dimensional black phosphorus-modified $\text{Cs}_2\text{AgBiBr}_6$ with efficient charge separation for enhanced visible-light photocatalytic $\text{H}_2$ evolution†

Kunpeng Song,<sup>a</sup>  <sup>ab</sup> Jiaojiao Gou,<sup>a</sup> Lin Wu<sup>a</sup> and Chunmei Zeng<sup>ab</sup>

Lead-free double halide perovskite ( $\text{Cs}_2\text{AgBiBr}_6$ ) is considered to be a potential candidate material for photocatalytic hydrogen production due to its excellent visible light capture capability. However, the rate of the hydrogen evolution reaction (HER) taking into account these catalysts is still insufficient. In this study, two-dimensional black phosphorus (BP) anchored on  $\text{Cs}_2\text{AgBiBr}_6$  (CABB) by electrostatic coupling was prepared. The resulting catalyst BP/CABB was quite stable in a HBr solution during the entire light reaction and reached a hydrogen production rate of  $104.6 \mu\text{mol h}^{-1} \text{g}^{-1}$  under visible light, which was higher than that of CABB alone. Significantly enhanced HER activity was explored by optical/photochemical measurements, indicating that BP can be used as an electronic accelerator, transmitted by a Z-scheme heterojunction in the interface of the catalyst to transfer electrons, and further produce hydrogen. This has been instrumental in the high-efficiency photocatalyst by anchoring the nonmetallic active sites on CABB.

Received 23rd July 2022,  
Accepted 15th September 2022

DOI: 10.1039/d2tc03100k

rsc.li/materials-c

### 1. Introduction

Energy and the environment are currently the two most important issues in society. With the development of technology and the varied demands of the world, the global energy crisis and various environmental issues have become increasingly severe.<sup>1–3</sup> Photocatalytic hydrogenation technology involving various semiconductor materials has attracted extensive attention as a clean and sustainable solar-hydrogen energy conversion technology.<sup>4–6</sup> Many efforts regarding photocatalytic hydrogen production technology are committed to utilizing low-cost and efficient photocatalysts. Although huge progress has been achieved, better candidates will always be sought. Among the various photocatalytic systems, the ideal photocatalyst should have a suitable optical bandgap and the ability to capture visible light and convert the absorbed solar energy into hydrogen energy.<sup>7</sup>

In recent years, due to their unique light absorption capacity and efficient charge separation properties, lead-based halide perovskites have become promising photocatalysts and have developed rapidly in the fields of  $\text{H}_2$  evolution, pollutant degradation, organic reactions, and carbon dioxide reduction.<sup>8–10</sup> However, the instability and ecological toxicity of lead-based

perovskites hinder their practical applications. In recent years, lead-free double perovskites have been studied gradually deepening, for example,  $\text{Cs}_3\text{Bi}_2\text{X}_9$  ( $\text{X} = \text{Cl}, \text{Br}, \text{I}$ ),  $(\text{MA})_3\text{Bi}_2\text{I}_9$ ,  $\text{DMASnBr}_3$ , and  $\text{Cs}_2\text{AgBiBr}_6$  (CABB).<sup>11–13</sup> Bi-based double perovskite CABB has shown potential in photocatalytic hydrogen production because of its good stability and suitable light absorption coefficient.<sup>14–16</sup> In 2018, Kuang *et al.* prepared CABB nanocrystals *via* a simple heat injection method and used them for photocatalytic  $\text{CO}_2$  reduction.<sup>17</sup> Zhao *et al.* constructed a  $\text{Cs}_2\text{AgBiBr}_6/\text{rGO}$  photocatalyst for  $\text{H}_2$  evolution by an *in situ* photoreduction method, reporting a photocatalytic system for the construction of a lead-free halide perovskite/semiconductor heterojunction.<sup>18</sup> Most recently, N-C,<sup>19</sup> Cu-RGO,<sup>20</sup> g- $\text{C}_3\text{N}_4$ ,<sup>21</sup>  $\text{MoS}_2$ ,<sup>22</sup> and  $\text{NiCoP}$ <sup>23</sup> have been exploited as costructures, and the obtained composites showed an obvious enhancement of photocatalytic activity compared to pristine CABB.

Two-dimensional black phosphorus (2D BP) with a large surface area, abundant active sites and adjustable band gaps (0.3–2.0 eV) is widely studied as a photocatalytic semiconductor catalyst.<sup>24,25</sup> In particular, BP exhibited excellent characteristics as a potential high-performance cocatalyst: (1) the large surface area has rich active sites, and the photocatalyst is structurally coupled electronically; (2) it has good carrier mobility; (3) the tunable bandgap provides a huge opportunity for a good structure. Shi's group<sup>26</sup> prepared black phosphorus quantum dot/CdS (BPQDS/CDS) composites with tight interfacial contact for efficient photocatalytic  $\text{H}_2$  evolution, benefiting from the strong interfacial interaction between CdS and BPQDS for efficient charge separation. Zhu and colleagues<sup>27</sup> anchored

<sup>a</sup> College of Chemistry and Chemical Engineering, China West Normal University, Shida Road, Nanchong, 637009, China. E-mail: song19880405@126.com, melzeng@163.com

<sup>b</sup> Chemical Synthesis and Pollution Control Key Laboratory of Sichuan Province, China West Normal University, Nanchong, 637009, China

† Electronic supplementary information (ESI) available. See DOI: <https://doi.org/10.1039/d2tc03100k>

inorganic perovskite ( $\text{CsPbBr}_3$ ) on BP to obtain a new effective  $\text{CsPbBr}_3/\text{BP}$  photocatalyst for  $\text{CO}_2$  reduction. The introduction of BP gave more active sites to promote the activation of  $\text{CO}_2$  reduction and capture excitation electrons of  $\text{CsPbBr}_3$  with high charge separation efficiency. Therefore, the use of BP as a metal-free costructure for photocatalytic  $\text{H}_2$  production is promising and challenging.

In this work, two-dimensional black phosphorus was first coupled with the CABB double perovskite applied for hydrobromic acid (HBr) splitting under visible light irradiation. Layered BP with good electron transfer properties and acid stability was introduced to further improve the  $\text{H}_2$  evolution. The  $\text{H}_2$  evolution rate of BP/CABB can reach  $104.6 \mu\text{mol h}^{-1} \text{g}^{-1}$ , which is 6 times higher than that of pristine CABB. Excitingly, the BP/CABB composites are quite stable in a saturated HBr solution, and their activity does not significantly decrease during the entire light reaction process. BP/CABB heterogeneous structures have good stability, providing new examples for the design and preparation of high-efficiency lead-free double perovskite catalysts.

## 2. Experiment

### 2.1 Photocatalyst synthesis

**2.1.1 Preparation of CABB.** CABB was synthesized from aqueous solution according to a previous report.<sup>14</sup> A total of 1.0 mmol  $\text{BiBr}_3$ , 1.0 mmol  $\text{AgBr}$ , and 2.0 mmol  $\text{CsBr}$  were dissolved in 10 mL of a 48% HBr solution, and then the mixture was heated to  $110^\circ\text{C}$  for 2 h under continuous magnetic stirring in an oil bath. After cooling to room temperature naturally, the precipitates were collected and dried in a vacuum oven at  $60^\circ\text{C}$  for 12 h, and the obtained orange sample was named CABB. As shown in Fig. 1, the saturated HBr solution (saturated with CABB power) for photocatalytic  $\text{H}_2$  evolution was prepared by mixing HBr and  $\text{H}_3\text{PO}_2$  at a volume ratio of 5 : 1.

**2.1.2 Preparation of BP.** BP was prepared with red phosphorus as the raw material and diethylenetriamine (DETA) as the solvent. In a typical synthesis process, red phosphorus (2.0 g, 0.06 mol) was added to an agate mortar and ground.

Then, the mixture with 40 mL deionized water (DI) was transferred to a 100 mL Teflon-lined stainless steel autoclave and heated at  $200^\circ\text{C}$  for 12 h. After cooling to room temperature, the mixture was washed, centrifuged, and dried overnight at  $60^\circ\text{C}$ , and the sample was labeled RP. Next, the prepared RP (0.90 g) was added to 60 mL of a DETA solution and was stirred for 30 min; the mixture was then heated at  $160^\circ\text{C}$  in a 100 mL Teflon-lined stainless steel autoclave for 24 h. After cooling to room temperature, the mixture was washed and centrifuged, and the product was collected and named BP.

**2.1.3 Preparation of BP/CABB composites.** We adjusted the mass ratio of the samples to achieve the optimum photocatalytic activity. Therefore, we conducted a series of experiments measuring the hydrogen evolution of the BP/CABB composite materials. Specifically, the prepared 50 mg CABB was first added to a saturated HBr aqueous solution, and then different BP mass ratios were added to the above solution and ultrasonicated for 20 min. During the precipitated crystalline cycle, the BP/CABB photocatalysts were obtained directly for photocatalytic hydrogenation or rinsed and dried to carry out further characterization. Samples were labeled as  $x\%$  BP/CABB ( $x = 5, 10, 15, 20$ ), where  $x$  is the mass percentage of BP and CABB. And the actual content of the catalyst 10% BP/CABB was also quantified by EDX testing (Table S1 and Fig. S1, ESI†).

### 2.2 Characterization

Powder X-ray diffraction (XRD) analysis was performed on a PANalytical X'pertProAlpha-1 X-ray diffractometer with  $\text{Cu K}\alpha$  radiation to explore the crystalline structure. The zeta potentials of the samples were measured on a Malvern zeta analyzer (Zetasizer Nano-S 90, Malvern Instrument, UK). Transmission electron microscopy (TEM) and high-resolution transmission electron microscopy (HRTEM) images were obtained on a JEOL JEM-2100 F electron microscope operated at an accelerating voltage of 200 kV. The UV-vis diffuse reflectance absorption spectrum (DRS) was measured using an ultraviolet-visible spectrophotometer (UV-3600, Shimadzu) with  $\text{BaSO}_4$  as a reference sample; X-ray photoelectron spectroscopy (XPS) was performed on a Thermo Scientific ESCALAB Xi +, the excitation

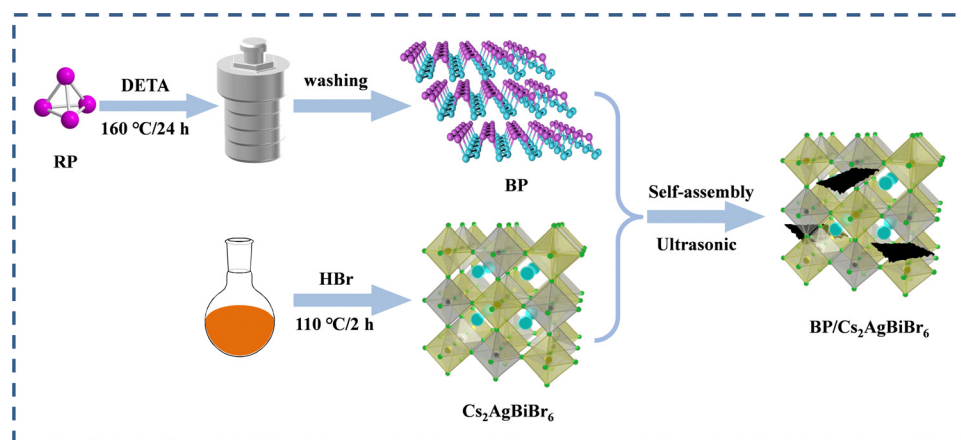


Fig. 1 Schematic diagram of the BP/CABB composite fabrication process.

source was monochromatic Al K $\alpha$ , and C 1s = 284.6 eV was used for reference calibration. Raman spectra were recorded on an Alpha 300 Access Raman microscope (Witec, Germany) with a 532 nm laser as an excitation source at room temperature.

### 2.3 Photocatalytic experiments

Photocatalytic H<sub>2</sub> production experiments were performed in an instrument equipped with a quartz vessel under the illumination of a 300 W Xe lamp ( $\lambda \geq 420$  nm). The BP/CABB photocatalyst (0.05 g) was added to 10 mL of CABB-saturated HBr/H<sub>3</sub>PO<sub>2</sub> solution, and the temperature of this mixture was maintained at 15 °C through a cooling water circulation system. The suspension extracted dissolved air before the reaction by a vacuum pump. After that, the reaction solution was irradiated to produce H<sub>2</sub> under continuous stirring. The amount of H<sub>2</sub> produced was automatically removed and analyzed at given time intervals with a CEL-SPH2N fully automatic online catalytic system (Beijing China Education Au-light Co., Ltd).

### 2.4 PEC measurements

The photocurrents and electrochemical impedance spectroscopy (EIS) profiles of the catalysts were evaluated using a standard three-electrode system (CHI760E), where a Pt electrode was used as the counter electrode, an Ag/AgCl electrode was used as the reference electrode, photocatalysts were coated on FTO (1 cm  $\times$  1 cm) as the working electrode, and 0.1 M tetrabutylammonium hexafluorophosphate (TBAPF<sub>6</sub>) in dichloromethane (CH<sub>2</sub>Cl<sub>2</sub>) was the electrolyte. The working electrode was prepared as follows: 10 mg samples were added to a mixture of 500  $\mu$ L absolute ethanol and 10  $\mu$ L Nafion and then sonicated for 60 min. Finally, a certain amount of the mixture was dripped onto FTO to prepare the working electrode.

## 3. Results and discussion

### 3.1 Structure, composition, and optical properties of the photocatalyst

To achieve large-scale and low-cost BP production, BP was prepared from bulk red phosphorus using a solvent thermal

reaction. After the solvent thermal reaction, the resulting solution was observed to become black, and a black product was obtained after washing. The X-ray diffraction pattern of the prepared BP powder sample showed the main features of orthogonal BP (PDF#76-1967); diffraction peaks located at 17.6°, 26.8°, 35.2°, and 57.2° correspond to the (020), (021), (040), and (151) crystalline planes, respectively (Fig. S2a, ESI†).<sup>28</sup> It is worth noting that the synthetic BP had an additional peak at 10.2° in the XRD pattern, which was due to a stacking breaking layer or periodic distortion in the *c*-axis direction.<sup>29</sup> Raman spectroscopy also confirmed the successful preparation of BP and composites. In Fig. S2b (ESI†), we recorded the Raman spectrum of BP and obtained three typical Raman peaks: A<sub>g</sub><sup>1</sup> (outdoor patterns), B<sub>2g</sub> and A<sub>g</sub><sup>2</sup> (in-plane mode), and the wavenumbers were  $\sim 361$ ,  $\sim 437$ , and  $\sim 460$  cm<sup>-1</sup>, respectively.<sup>30</sup> These results suggest that this bottom-up solvothermal method is a reliable method for preparing large-scale and low-cost BP.

To verify the structural stability of the BP, we tested the XRD of the prepared BP after 12 h of stirring in a HBr solution. As shown in Fig. S3a (ESI†), the structure of BP did not change significantly after HBr treatment, but the intensity of the diffraction peak was reduced, which is possibly due to BP oxidation by the environment. As seen in Fig. S3b (ESI†), CABB and BP had zeta potentials of -16.4 mV and 8.98 mV, respectively. The opposite potentials generate strong electrostatic attraction between CABB and BP, which increases interfacial contacts. We used the ultrasonic electrostatic self-assembly method to prepare a series of *x*% BP/CABB composites. As seen in Fig. 2a, the XRD of the BP/CABB composites showed all the characteristic peaks of CABB with a good cubic structure. The characteristic diffraction peaks were located at 13°, 15.9°, 22.3°, 26.1°, 27.4°, 31.8°, 35.7°, 39.2° and 45.5° belonging to the (111), (002), (022), (113), (222), (004), (024), (224) and (440) planes, respectively (JCPDS # 01-084-8699).<sup>20</sup> No additional diffraction peaks attributed to BP were observed even at higher addition amounts, probably due to the high dispersion of BP and the high crystallinity of CABB.<sup>31–33</sup> The presence of BP in the composites was also confirmed by comparing the UV-visible diffuse spectra (DRS) of the original BP, CABB and BP/CABB composites. As shown in Fig. 2b, the light absorption of the BP/

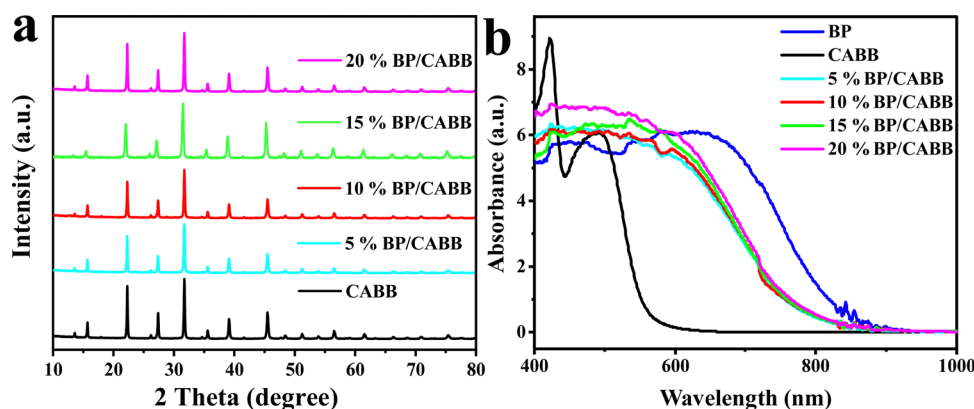


Fig. 2 (a) XRD and (b) DRS patterns of the obtained CABB, BP and BP/CABB.

CABB composite was enhanced between 600 and 750 nm relative to the original CABB due to the black effect of the BP. With the increase of black phosphine loading, the optical absorption intensity of the composite material also increased, but the increase amount changed little.

To clarify the interface interactions in BP/CABB, TEM and SEM images were obtained, and the corresponding elemental mapping analysis was performed. The original CABB particles had a relatively smooth and large bulk, and BP showed a laminate stacked structure (Fig. S43a and b, ESI†). The surface of the BP/CABB composite becomes rougher due to the coupling of layered BP (Fig. 3a). Thus, more contact sites in the reaction are provided. The TEM image of composite BP/CABB showed small, layered BP in close contact with large CABB particles (Fig. 3b), and the size of the BP was approximately 500 nm. The EDS mappings (Fig. 3c) of composite BP/CABB confirmed the uniform distribution of Cs, Ag, Bi, Br, and P elements on the catalyst surface. In the high-resolution TEM image (Fig. 3d), two different lattice fringes of 0.33 nm and 0.23 nm were present, corresponding to the (021) plane of BP and the (004) plane of CABB, respectively. The TEM images show that the composites are tightly bound together; in particular, the high-resolution TEM images (Fig. S4c and d, ESI†) show that BP and CABB are embedded together rather than physically adsorbed. These results revealed the successful coupling of CABB with BP.

X-Ray photoelectron spectroscopy (XPS) was further used to explore the chemical state of the resulting BP, CABB and CABB/CABB composites. The XPS survey spectra (Fig. 4a) confirmed the presence of BP in the BP/CABB composites. As shown in Fig. 4b, Cs 3d can be divided into two peaks at 723.9 eV and 739.9 eV, corresponding to Cs 3d<sub>5/2</sub> and Cs 3d<sub>3/2</sub>, respectively. Ag 3d can be divided into peaks located at 367.5 eV and 373.6 eV,

corresponding to Ag 3d<sub>5/2</sub> and Ag 3d<sub>3/2</sub>, respectively (Fig. 4c). As shown in Fig. 4d, Bi 4f can be divided into two peaks located at 158.7 eV and 164.1 eV, corresponding to Bi 4f<sub>7/2</sub> and Bi 4f<sub>5/2</sub>, respectively. Br 3d can be divided into two peaks located at 67.2 eV and 68.3 eV, corresponding to Br 3d<sub>5/2</sub> and Br 3d<sub>3/2</sub>, respectively (Fig. 4e). Interestingly, Bi 4f is shifted to a lower binding energy (0.3 eV) (Fig. 4d), while the P 2p peaks migrate to a higher binding energy (0.5 eV) (Fig. 4f). The study shows that the binding energy migration is closely related to the electron density outside the nucleus. When the binding energy is shifted to a high field, the electron density decreases.<sup>34</sup> This is consistent with the results reported in the literature.<sup>21,35,36</sup> The binding energy migration of P and Bi greatly confirms the strong electronic coupling between BP and CABB, which is in accordance with the Raman spectroscopy results. It is worth noting that a small P oxide species is apparent at 134 eV due to the inevitable local oxidation during the preparation process. All the results show that the prepared BP/CABB composite has a strong interfacial electron coupling rather than simple physical mixing, which is very beneficial to the efficient migration of interfacial carriers.

### 3.2 Photocatalytic hydrogenation activity

The photocatalyst was evolved in a saturated HBr/H<sub>3</sub>PO<sub>2</sub> mixed solution (v/v = 5:1) under visible light irradiation, and the photocatalytic H<sub>2</sub> evolution activity of the different catalysts is shown in Fig. 5a. Bare BP (50 mg) showed little H<sub>2</sub> evolution activity, while CABB (50 mg) showed an H<sub>2</sub> evolution rate of 17.7 μmol g<sup>-1</sup> h<sup>-1</sup>, which was extremely low due to the rapid recombination of photogenerated electron-hole pairs. As the amount of BP added to the BP/CABB increased, the hydrogen production rate was further improved, and the catalyst 10% BP/CABB composite gave the best rate of 104.6 μmol h<sup>-1</sup> g<sup>-1</sup>, which was 6 times higher than that of pristine CABB. When the

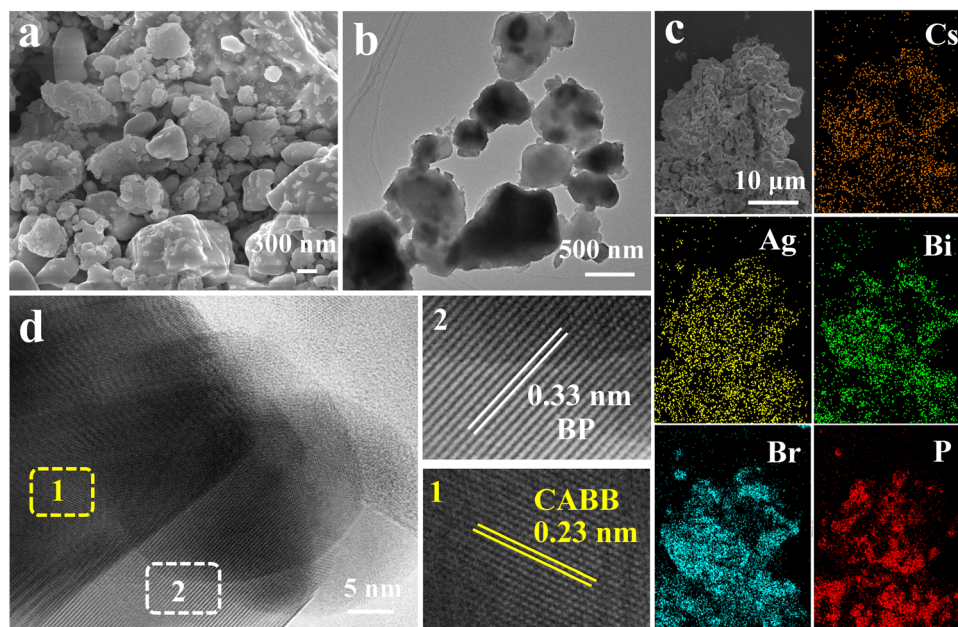


Fig. 3 (a) SEM image, (b) TEM image, (c) elemental mapping of Cs, Ag, Bi, Br and P and (d) HRTEM images of the 10% BP/CABB composite.



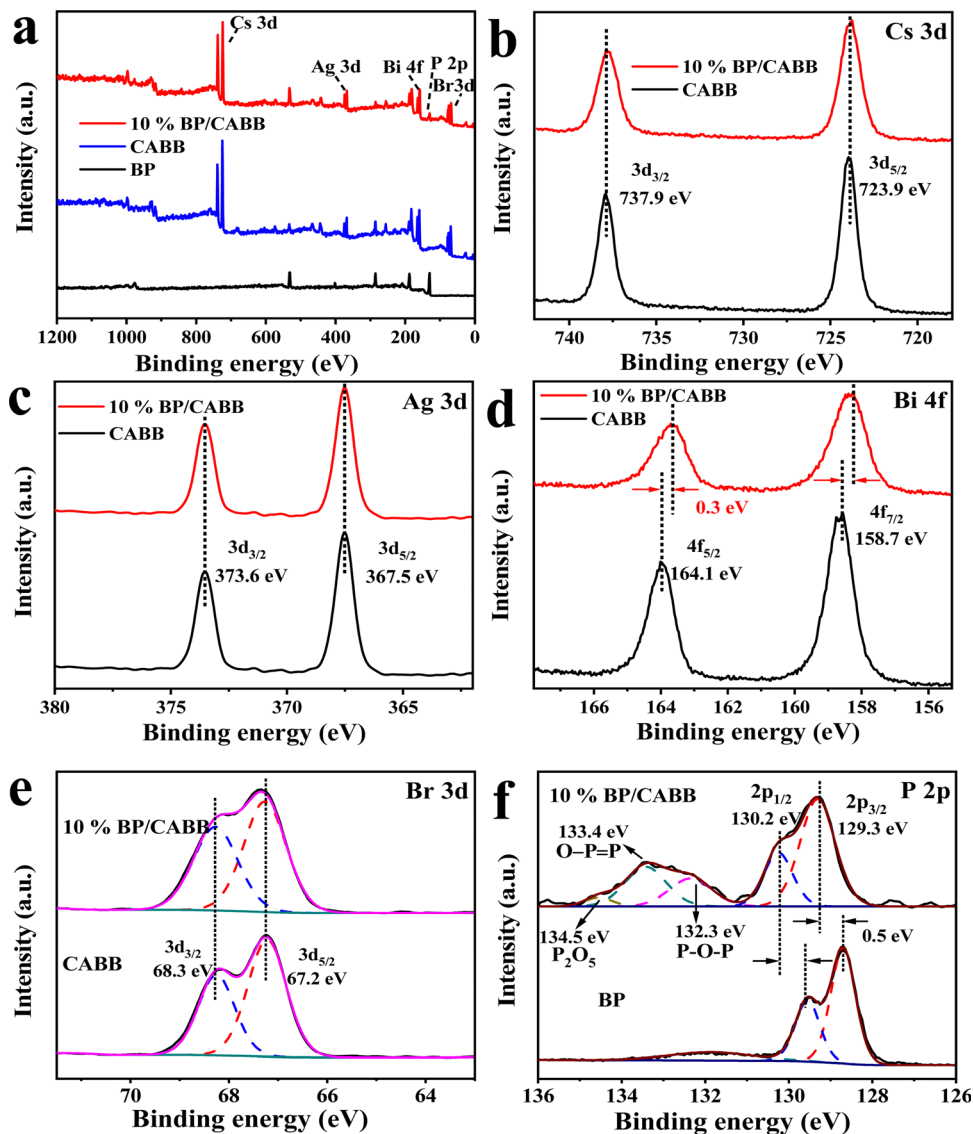


Fig. 4 (a) Survey XPS spectra of CABB, BP and the 10% BP/CABB composite; high-resolution XPS spectrum of (b) Cs 3d, (c) Ag 3d, (d) Br 3d, (e) Bi 4f and (f) P 2p.

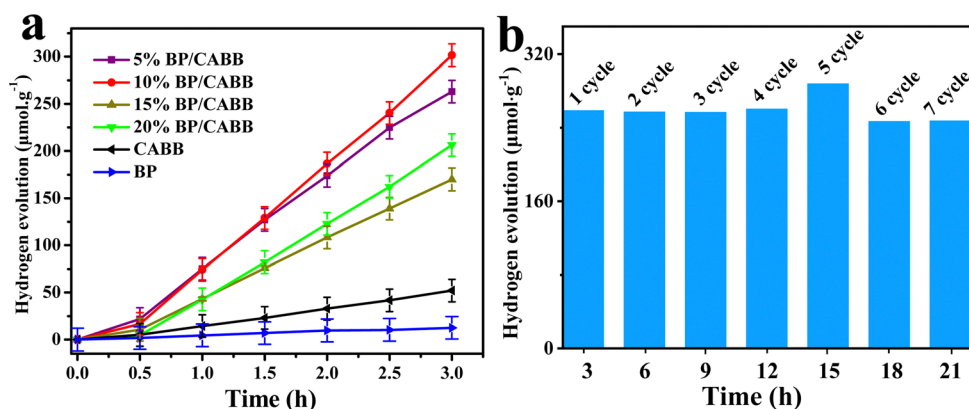


Fig. 5 (a) Yield of H<sub>2</sub> reduction by CABB, BP and the 10% BP/CABB composite after 3 h of photochemical reaction, error bar:  $\pm 0.03$ ; and (b) recycling test of the 10% BP/CABB composite.

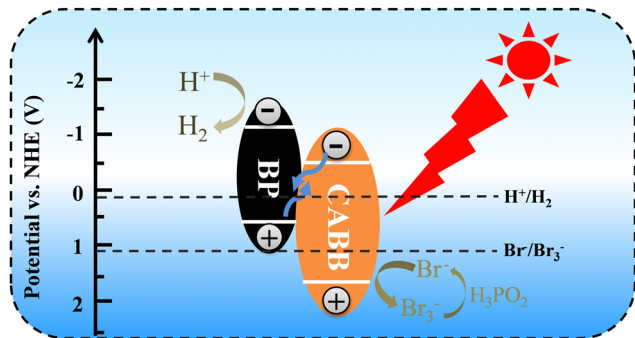


Fig. 6 Schematic illustration of the  $\text{H}_2$  evolution of the BP/CABB composites.

BP addition further increased to 15%, the incident light was blocked by excess BP, resulting in a decrease in photocatalytic activity. The results showed that BP can show photocatalytic  $\text{H}_2$  evolution under visible light as a highly active cocatalyst of CABB.

Cyclic performance is an important index for evaluating heterogeneous catalysts. In this catalytic system, no significant decline in  $\text{H}_2$  evolution was observed after 7 cycles of 3 h of continuous photoreaction (Fig. 5b). After being reused, the catalyst showed no crystallographic phase change in the XRD pattern (Fig. S5, ESI†). The good structural stability of BP/CABB composites can be rationalized, and CABB surfaces can constantly resume sustained oxidation of  $\text{Br}^-$ – $\text{Br}_3^-$  due to the perfect dynamic equilibrium of the CABB crystal in a saturated aqueous solution. Therefore, both CABB and BP in the composite material were highly stable due to the strong interaction. BP, as a photosensitizer and  $\text{H}_2$  evolution cocatalyst, also enhanced the efficient and sustainable photocatalytic  $\text{H}_2$  evolution.

### 3.3 Activation mechanism

We studied the photocatalytic mechanism of the BP/CABB system by optical absorption and valence band (VB) XPS. According to the Tauc plot method,  $(\alpha h\nu)^{1/n} = A(h\nu - E_g)$ , where the direct bandgap semiconductor is  $n = 1/2$  and the indirect bandgap semiconductor is  $n = 2$ . BP is a direct band gap semiconductor, CABB is an indirect bandgap semiconductor, and the  $E_g$  values of BP and CABB were

calculated to be 1.57 V and 2.15 V, respectively (Fig. S6a and b, ESI†). The calculated value of BP and CABB from the intercept between the tangent of the onset and the baseline of the spectra is 0.50 V and 1.69 V, respectively (Fig. S6c and d, ESI†). This is consistent with the reported valence band position ( $E_{\text{VB}}$ ).<sup>21,37</sup> Based on the relationships between  $E_{\text{CB}}$  and  $E_{\text{VB}}$  ( $E_{\text{CB}} = E_{\text{VB}} - E_g$ ), the calculated conduction band positions ( $E_{\text{CB}}$ ) for BP and CABB were  $-1.07$  V and  $-0.46$  V.<sup>26</sup> Based on the above results, a photocatalytic mechanism was proposed (Fig. 6). According to the  $\text{H}_2$  evolution “band matching” theory, the  $E_{\text{CB}}$  of BP is more negative than CABB, and the  $E_{\text{VB}}$  of CABB is more positive than BP. When both BP and CABB were excited under visible light irradiation, the photogenerated electrons in the CB of CABB quickly combined with the photogenerated holes in the VB of BP and then combined with the photogenerated electrons of BP for the reduction reaction. The photogenerated holes in the VB of CABB are used for the oxidation reaction. These band structures suggest the possibility of constructing the Z-scheme photocatalysis feature to split HBr into  $\text{H}_2$  and  $\text{Br}_3^-$ , where  $\text{Br}_3^-$  is then converted to  $\text{Br}^-$  by  $\text{H}_3\text{PO}_3$ .

Photoelectric chemistry (PEC) analysis is widely used to provide effective evidence for the separation and metastasis of photogenerated electron–hole pairs. To explore the mechanism of BP effect on the photocatalytic activity on CABB, we performed a series of PEC measurements. BP/CABB exhibited a higher photocurrent response than bare CABB (Fig. 7a), and the photocurrent responses of the samples were highly repeatable upon on/off light cycling. This indicated the efficient separation of carriers in BP/CABB. Electrochemical impedance spectroscopy (EIS) measurements (Fig. 7b) indicated that BP/CABB had a smaller charge transfer resistor than the bare CABB, indicating that the coupled BP provides a rapid electron transfer pathway to improve charge separation efficiency. All the results demonstrated that coupling with BP can significantly increase the carrier separation efficiency of CABB, which greatly increases the photocatalytic efficiency of BP/CABB.

## 4. Conclusions

In summary, we successfully fabricated 2D BP/CABB composites with a high-quality interface *via* a facile electrostatic

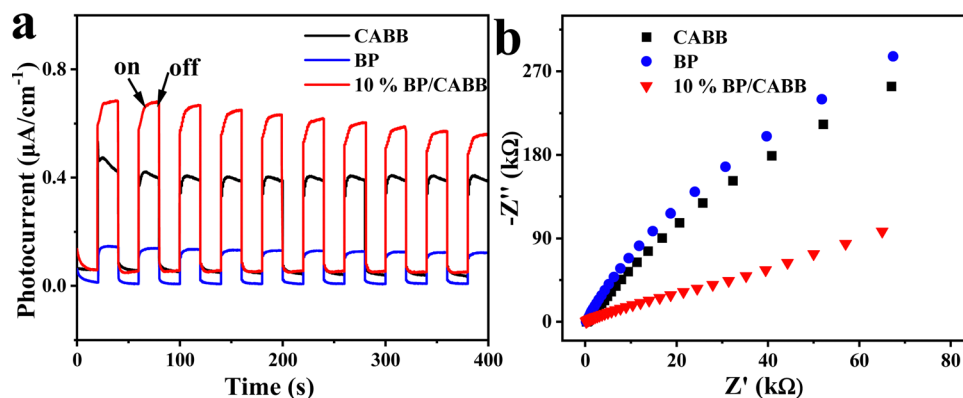


Fig. 7 (a) Chopped light amperometric  $I$ – $t$  curves and (b) EIS Nyquist plots of CABB, BP and the 10% BP/CABB composite.

self-assembly method. The  $H_2$  evolution rate of the most effective BP/CABB composite was 6 times higher than that of the original CABB and had excellent  $H_2$  evolution stability. In the BP/CABB composites, the charge induction between BP and CABB made the interface interaction strong, which can realize efficient charge separation and improve the photocatalytic  $H_2$  evolution activity. This work demonstrates a simple and effective strategy for the synthesis of BP/CABB composites with high-quality interactions. This study also provides new insight into the design of highly active photocatalysts based on lead-free double halides.

## Author contributions

Kunpeng Song: guidance of experimental projects, revision and submission of papers; Jiaojiao Gou: experiment and the writing of the draft; Lin Wu: experiment; Chunmei Zeng: design of the experimental projects.

## Conflicts of interest

The authors declare that they have no known competing financial interests or personal relationships that could have appeared to influence the work reported in this paper.

## Acknowledgements

This work was supported by the Key Program of Sichuan Provincial Department of Education (16ZA0176) and the Fundamental Research Funds of China West Normal University (17C037 and 15E005).

## References

- 1 J. Ran, J. Zhang, J. Yu, M. Jaroniec and S. Z. Qiao, Earth-abundant cocatalysts for semiconductor-based photocatalytic water splitting, *Chem. Soc. Rev.*, 2014, **43**, 7787–7812.
- 2 X. Zou and Y. Zhang, Noble metal-free hydrogen evolution catalysts for water splitting, *Chem. Soc. Rev.*, 2015, **44**, 5148–5180.
- 3 R. Schlögl, Chemical energy storage enables the transformation of fossil energy systems to sustainability, *Green Chem.*, 2021, **23**, 1584–1593.
- 4 Z. Abidin, A. Zafaranloo, A. Rafiee, W. Mérida, W. Lipiński and K. R. Khalilpour, Hydrogen as an energy vector, *Renewable Sustainable Energy Rev.*, 2020, **120**, 109620.
- 5 F. Dawood, M. Anda and G. M. Shafiullah, Hydrogen production for energy: An overview, *Int. J. Hydrogen Energy*, 2020, **45**, 3847–3869.
- 6 S. Liu, M. W. Heindl, N. Fehn, S. Caicedo-Davila, L. Eyre, S. M. Kronawitter, J. Zerhoch, S. Bodnar, A. Shcherbakov, A. Stadlbauer, G. Kieslich, I. D. Sharp, D. A. Egger, A. Kartouzian and F. Deschler, Optically Induced Long-Lived Chirality Memory in the Color-Tunable Chiral Lead-Free Semiconductor (R)/(S)-CHEA<sub>4</sub>Bi<sub>2</sub>Br<sub>x</sub>I<sub>10-x</sub> (x = 0–10), *J. Am. Chem. Soc.*, 2022, **144**, 14079–14089.
- 7 C. Xia, H. Wang, J. K. Kim and J. Wang, Rational Design of Metal Oxide-Based Heterostructure for Efficient Photocatalytic and Photoelectrochemical Systems, *Adv. Funct. Mater.*, 2021, **31**, 2008247.
- 8 W. Song, Y. Wang, C. Wang, B. Wang, J. Feng, W. Luo, C. Wu, Y. Yao and Z. Zou, Photocatalytic Hydrogen Production by Stable CsPbBr<sub>3</sub>@PANI Nanoparticles in Aqueous Solution, *ChemCatChem*, 2021, **13**, 1711–1716.
- 9 Z. Zhang, M. Shu, Y. Jiang and J. Xu, Fullerene modified CsPbBr<sub>3</sub> perovskite nanocrystals for efficient charge separation and photocatalytic CO<sub>2</sub> reduction, *Chem. Eng. J.*, 2021, **414**, 128889.
- 10 Y. Zhao, Y. Dai, Q. Wang, Y. Dong, T. Song, A. Mudryi, Q. Chen and Y. Li, Anions-Exchange-Induced Efficient Carrier Transport at CsPbBr<sub>3</sub>Cl<sub>3-x</sub>/TiO<sub>2</sub> Interface for Photocatalytic Activation of C(sp<sup>3</sup>)-H bond in Toluene Oxidation, *ChemCatChem*, 2021, **13**, 2592–2598.
- 11 L. Malavasi, L. Romani, A. Speltini, F. Ambrosio, E. Mosconi, A. Profumo, S. Margadonna, A. Milella, F. Fracassi, A. Listorti, F. De Angelis and M. Marelli, Water-Stable DMASnBr<sub>3</sub> Lead-Free Perovskite for Effective Solar-Driven Photocatalysis, *Angew. Chem., Int. Ed.*, 2020, **133**, 3655–3662.
- 12 L. Romani, A. Speltini, C. N. Dibenedetto, A. Listorti, F. Ambrosio, E. Mosconi, A. Simbula, M. Saba, A. Profumo, P. Quadrelli, F. De Angelis and L. Malavasi, Experimental Strategy and Mechanistic View to Boost the Photocatalytic Activity of Cs<sub>3</sub>Bi<sub>2</sub>Br<sub>9</sub> Lead-Free Perovskite Derivative by g-C<sub>3</sub>N<sub>4</sub> Composite Engineering, *Adv. Funct. Mater.*, 2021, **31**, 2104428.
- 13 Y. Tang, C. H. Mak, R. Liu, Z. Wang, L. Ji, H. Song, C. Tan, F. Barrière and H. Y. Hsu, In Situ Formation of Bismuth-Based Perovskite Heterostructures for High-Performance Cocatalyst-Free Photocatalytic Hydrogen Evolution, *Adv. Funct. Mater.*, 2020, **16**(836), 2006919.
- 14 A. H. Slavney, T. Hu, A. M. Lindenberg, H. I. Karunadasa and A. Bismuth-Halide, Double Perovskite with Long Carrier Recombination Lifetime for Photovoltaic Applications, *J. Am. Chem. Soc.*, 2016, **138**, 2138–2141.
- 15 Z. Xiao, W. Meng, J. Wang and Y. Yan, Thermodynamic Stability and Defect Chemistry of Bismuth-Based Lead-Free Double Perovskites, *ChemSusChem*, 2016, **9**, 2628–2633.
- 16 N. Hao, Y. Qiu, J. W. Lu, X. Han, Y. Q. Li, J. Qian and K. Wang, Flexibly regulated electrochemiluminescence of all-inorganic perovskite CsPbBr<sub>3</sub> quantum dots through electron bridge to across interfaces between polar and non-polar solvents, *Chin. Chem. Lett.*, 2021, **32**, 2861–2864.
- 17 L. Zhou, Y. F. Xu, B. X. Chen, D. B. Kuang and C. Y. Su, Synthesis and Photocatalytic Application of Stable Lead-Free Cs<sub>2</sub>AgBiBr<sub>6</sub> Perovskite Nanocrystals, *Small*, 2018, **14**, 1703762.
- 18 T. Wang, D. Yue, X. Li and Y. Zhao, Lead-free double perovskite Cs<sub>2</sub>AgBiBr<sub>6</sub>/RGO composite for efficient visible light photocatalytic H<sub>2</sub> evolution, *Appl. Catal., B*, 2020, **268**, 118399.
- 19 Y. Jiang, K. Li, X. Wu, M. Zhu, H. Zhang, K. Zhang, Y. Wang, K. P. Loh, Y. Shi and Q.-H. Xu, In Situ Synthesis of Lead-Free

- Halide Perovskite  $\text{Cs}_2\text{AgBiBr}_6$  Supported on Nitrogen-Doped Carbon for Efficient Hydrogen Evolution in Aqueous HBr Solution, *ACS Appl. Mater. Interfaces*, 2021, **13**, 10037–10046.
- 20 S. Kumar, I. Hassan, M. Regue, S. Gonzalez-Carrero, E. Rattner, M. A. Isaacs and S. Eslava, Mechanochemically synthesized Pb-free halide perovskite-based  $\text{Cs}_2\text{AgBiBr}_6$ -Cu-RGO nanocomposite for photocatalytic  $\text{CO}_2$  reduction, *J. Mater. Chem. A*, 2021, **9**, 12179–12187.
  - 21 Y. Wang, H. Huang, Z. Zhang, C. Wang, Y. Yang, Q. Li and D. Xu, Lead-free perovskite  $\text{Cs}_2\text{AgBiBr}_6$ @g- $\text{C}_3\text{N}_4$  Z-scheme system for improving  $\text{CH}_4$  production in photocatalytic  $\text{CO}_2$  reduction, *Appl. Catal., B*, 2021, **282**, 119570.
  - 22 Y. Zhang, Z. Sun, Z. Wang, Y. Zang and X. Tao, Efficient and long-term photocatalytic  $\text{H}_2$  evolution stability enabled by  $\text{Cs}_2\text{AgBiBr}_6/\text{MoS}_2$  in aqueous HBr solution, *Int. J. Hydrogen Energy*, 2022, **47**, 8829–8840.
  - 23 Q. Huang, Y. Guo, J. Chen, Y. Lou and Y. Zhao, NiCoP modified lead-free double perovskite  $\text{Cs}_2\text{AgBiBr}_6$  for efficient photocatalytic hydrogen generation, *New J. Chem.*, 2022, **46**, 7395–7402.
  - 24 N. V. Chien, H. Shin and J. Y. Song, Sn-assisted solid state crystallization of red phosphorus to black phosphorus, *Scr. Mater.*, 2020, **177**, 128–131.
  - 25 L. Zhang, Z.-Q. Wang, J. Liao, X. Zhang, D. Feng, H. Deng and C. Ge, Infrared-to-visible energy transfer photocatalysis over black phosphorus quantum dots/carbon nitride, *Chem. Eng. J.*, 2022, **431**, 133453.
  - 26 F. Liu, Z. Wang, Y. Weng, R. Shi, W. Ma and Y. Chen, Black Phosphorus Quantum Dots Modified CdS Nanowires with Efficient Charge Separation for Enhanced Photocatalytic  $\text{H}_2$  Evolution, *ChemCatChem*, 2021, **13**, 1355–1361.
  - 27 X. Wang, J. He, J. Li, G. Lu, F. Dong, T. Majima and M. Zhu, Immobilizing perovskite  $\text{CsPbBr}_3$  nanocrystals on Black phosphorus nanosheets for boosting charge separation and photocatalytic  $\text{CO}_2$  reduction, *Appl. Catal., B*, 2020, **277**, 119230.
  - 28 Y. Wang, M. He, S. Ma, C. Yang, M. Yu, G. Yin and P. Zuo, Low-Temperature Solution Synthesis of Black Phosphorus from Red Phosphorus: Crystallization Mechanism and Lithium Ion Battery Applications, *J. Phys. Chem. Lett.*, 2020, **11**, 2708–2716.
  - 29 A. Ozawa, M. Yamamoto, T. Tanabe, S. Hosokawa and T. Yoshida, Black phosphorus synthesized by solvothermal reaction from red phosphorus and its catalytic activity for water splitting, *J. Mater. Chem. A*, 2020, **8**, 7368–7376.
  - 30 S. Zhu, Q. Liang, Y. Xu, H. Fu and X. Xiao, Facile Solvothermal Synthesis of Black Phosphorus Nanosheets from Red Phosphorus for Efficient Photocatalytic Hydrogen Evolution, *Eur. J. Inorg. Chem.*, 2020, 773–779.
  - 31 Y. Wu, P. Wang, X. Zhu, Q. Zhang, Z. Wang, Y. Liu, G. Zou, Y. Dai, M.-H. Whangbo and B. Huang, Composite of  $\text{CH}_3\text{NH}_3\text{PbI}_3$  with Reduced Graphene Oxide as a Highly Efficient and Stable Visible-Light Photocatalyst for Hydrogen Evolution in Aqueous HI Solution, *Adv. Mater.*, 2018, **30**, 1704342.
  - 32 R. Li, X. Li, J. Wu, X. Lv, Y.-Z. Zheng, Z. Zhao, X. Ding, X. Tao and J.-F. Chen, Few-layer black phosphorus-on- $\text{MAPbI}_3$  for superb visible-light photocatalytic hydrogen evolution from HI splitting, *Appl. Catal., B*, 2019, **259**, 118075.
  - 33 Z. Zhao, J. Wu, Y.-Z. Zheng, N. Li, X. Li and X. Tao,  $\text{Ni}_3\text{C}$ -Decorated  $\text{MAPbI}_3$  as Visible-Light Photocatalyst for  $\text{H}_2$  Evolution from HI Splitting, *ACS Catal.*, 2019, **9**, 8144–8152.
  - 34 M. Zhu, Z. Sun, M. Fujitsuka and T. Majima, Z-Scheme Photocatalytic Water Splitting on a 2D Heterostructure of Black Phosphorus/Bismuth Vanadate Using Visible Light, *Angew. Chem., Int. Ed.*, 2018, **57**, 2160–2164.
  - 35 Y. Jiang, H.-Y. Chen, J.-Y. Li, J.-F. Liao, H.-H. Zhang, X.-D. Wang and D.-B. Kuang, Z-Scheme 2D/2D Heterojunction of  $\text{CsPbBr}_3/\text{Bi}_2\text{WO}_6$  for Improved Photocatalytic  $\text{CO}_2$  Reduction, *Adv. Funct. Mater.*, 2020, **30**, 2004293.
  - 36 Z. Chen, Y. Hu, J. Wang, Q. Shen, Y. Zhang, C. Ding, Y. Bai, G. Jiang, Z. Li and N. Gaponik, Boosting Photocatalytic  $\text{CO}_2$  Reduction on  $\text{CsPbBr}_3$  Perovskite Nanocrystals by Immobilizing Metal Complexes, *Chem. Mater.*, 2020, **32**, 1517–1525.
  - 37 B. Tian, B. Tian, B. Smith, M. C. Scott, Q. Lei, R. Hua, Y. Tian and Y. Liu, Facile bottom-up synthesis of partially oxidized black phosphorus nanosheets as metal-free photocatalyst for hydrogen evolution, *Proc. Natl. Acad. Sci. U. S. A.*, 2018, **115**, 4345–4350.